Journal of Alloys and Compounds 509 (2011) 6364–6373

Contents lists available at ScienceDirect

Journal of Alloys and Compounds

journal homepage: www.elsevier.com/locate/jallcom

Microstructural evolution and mechanical, and corrosion property evaluation of Cu–30Ni alloy formed by Direct Metal Deposition process

S. Bhattacharya[a,*], G.P. Dinda[b], A.K. Dasgupta[b], H. Natu[c], B. Dutta[c], J. Mazumder[a,c]

[a] *University of Michigan, 2350 Hayward Street, 2040 G.G. Brown Laboratories, Ann Arbor, MI 48109, USA*
[b] *Center for Advanced Technologies, Focus: HOPE, Detroit, MI 48238, USA*
[c] *The POM Group Inc., Auburn Hills, MI 48326, USA*

ARTICLE INFO

Article history:
Received 13 January 2011
Received in revised form 14 March 2011
Accepted 16 March 2011
Available online 9 April 2011

Keywords:
Direct Metal Deposition
Dendrites
Dendrite arm spacing
Lattice parameters
Ultimate tensile strength
Yield strength
Percentage elongation
Corrosion resistance

ABSTRACT

In the current investigation Cu–30Ni alloy was successfully laser deposited on a rolled C71500 plate substrate by Direct Metal Deposition technology. The microstructural investigation of the clad was performed using optical and scanning electron microscopy. The phase and crystal structure analysis was performed using X-ray diffraction technique and transmission electron microscopy. The microstructure consisted of columnar and equiaxed dendrites with face centered cubic crystal structure. The dendrites grew epitaxially from the substrate and layer and bead boundaries. Dendrites' growth direction $\langle 0\,0\,1\rangle$ and growth angle 60° was maintained in each layer. The average primary dendritic arm spacing at the bottom part of the layers was about 7.5 μm and average secondary dendritic arm spacing in the upper part of the layer varied between 2 μm and 4.5 μm. The lattice parameter of the identified phase was found to be longer than that reported in literature. The reported lattice parameters in literature are however from samples processed under equilibrium conditions. The microhardness of the clad was found to be less than the substrate but very consistent along the clad. Cu–30Ni clad specimen showed higher ultimate tensile strength but lower yield strength and percentage elongation as compared to the C71500 substrate. DMD Cu–30Ni clad/C71500 substrate specimen showed the worst mechanical properties. The corrosion resistance of the specimens was found to decrease in the order DMD Cu–30Ni clad, half-and-half DMD Cu–30Ni clad-C71500 substrate, and C71500 substrate.

1. Introduction

Direct Metal Deposition (DMD), developed at the University of Michigan Ann Arbor, is a manufacturing process involving rapid solidification [1–3] and has been shown to minimize segregation of phases, extend solid solubility of alloying elements and produce fine grains which resulted in improving the mechanical properties of the materials [1–5]. DMD and several similar technologies namely, Directed Light Fabrication (DLF®) [6], Laser Engineered net Shaping (LENS®) [7], and Selective Laser Sintering (SLS®) [8] fall under a new group of manufacturing technologies called solid free form fabrication (SFF). SFF technologies are additive processes and include rapid prototyping (RP) and rapid manufacturing (RM) to produce near-net shape components from their computer aided design (CAD) files [2,9].

In DMD a CAD model is used for RP of the 3D object to be built. The entire 3D CAD model is divided into several 2-D parallel slices, each with a build height of approximately 25–33% of the beam diameter, and then a tool path is created to build each layer. The tool path data is converted into conventional CNC G and M codes and fed into the computer. RM then follows by focusing a high power laser beam onto a substrate to create a melt pool and simultaneously delivering fused pure metal (or alloy) powders into the melt pool through a specially designed coaxial nozzle, and forming a metallurgical bond with the substrate. The 3D object is created layer by layer by using a CNC machine that controls the part geometry and layer height according to the tool path data fed to the computer [10]. DMD has an edge over conventional manufacturing processes for low volume manufacturing of near-net shape components with complex geometries, coating surfaces, repairing parts, and building graded materials [2] .The closed loop optical feedback system employed in the DMD process reduces the manufacturing time, by eliminating intermediate steps from design to product [3]. The closely controlled process parameters during DMD also produces clad with uniform thickness and extremely fine and controlled microstructure [2–4]. However during DMD due to rapid solidification residual stresses are generated [11] which could result in cracks formation in the clad.

---

[*] Corresponding author. Tel.: +1 734 764 2177; fax: +1 734 763 5772.
E-mail addresses: sudipb@umich.edu, sudip.bhattacharya@gmail.com (S. Bhattacharya).

0925-8388/$ – see front matter © 2011 Elsevier B.V. All rights reserved.
doi:10.1016/j.jallcom.2011.03.091

Table 1
Cu–30Ni alloy powder composition (wt%).

Cu	Ni	Fe	Mn	Zn	C	Pb	P	S
Bal.	29.0–33.0	0.4–1.0	1.0	0.5 max	0.45	0.02 max	0.02 max	0.02 max

Copper based alloys generally have low strength but it has been shown that with different manufacturing techniques and alloying additions superior mechanical and corrosion resistance properties have been realized. Cupro–nickel alloys (primarily Cu–10Ni or Cu–30Ni, with compositions in approximate weight percentages) with some minor alloying additions are widely utilized as engineering materials for making condenser tubes of ships, heat exchangers of coastal power plants, desalination apparatuses and pipelines of desalination plants, boat hulls and several marine engineering applications because of their good corrosion resistance, good ductility, excellent electrical and thermal conductivity and superior anti fouling properties in seawater [12–15]. Minor iron additions, up to 1.8%, to cupro–nickel alloys have been reported to enhance the corrosion resistance of these alloys. It has been shown that the addition of iron both in and out of the copper–nickel solid solution increases the corrosion resistance in two ways. First in the solid solution, iron ions acts as an additional dopant to the protective Cu_2O film and enhances the stress corrosion resistance of the alloy. Second, complex iron phases formed on the protective Cu_2O film also helps in reducing the corrosion rate of these alloys [14–18]. However, excess precipitation of iron from the solid solution reduces the stress corrosion resistance of these alloys by reducing the iron content available for doping the protective Cu_2O film [14,18]. Iron addition of more than 2% also decreases the corrosion resistance of the cupro–nickel alloys [16]. Addition of other alloying additions in excess besides the usual iron addition up to 1.8% has been reported to be detrimental to the mechanical and corrosion properties of the alloys. Excess alloying additions cause severe segregation and coarsening of the microstructure in alloys produced by conventional casting [15,19]. The microstructure could be homogenized by subsequent annealing and has been shown to improve the mechanical and corrosion properties but are usually time consuming [12,13]. Cupro–nickel alloys produced by rapid solidification techniques such as, planar flow castings and melt spinning have been reported to have better corrosion resistance and mechanical properties compared to those produced by conventional casting. This has been attributed to fine grain size, homogeneous chemical composition and elimination of coarse segregated phases [15,19–21].

Since cupro–nickel alloys are primarily used as marine engineering material, failure of the equipments built with these alloys has been reported to occur primarily due to (i) stress corrosion caused by sulphide or ammonia polluted sea water, (ii) erosion corrosion caused by excessive fluid flow velocities and (iii) crevice or pitting corrosion [1,12,16] in seawater. Corrosion resistances of cupro–nickel alloys are typically compared by (i) weight loss measurements as a function of time and (ii) electrochemical measurements to measure the potentiodynamic polarization of test specimens in artificial or natural seawater solutions [12–14,16,20,22]. During the test, seawater solutions were maintained at a slightly higher temperature and specimens were immersed either in a static bath [1] or in an agitated bath, either by moving the specimen at certain velocity or by aerating the solution to simulate the seawater corrosion [13,14,16,20].

The current research effort was undertaken to repair some high value C71500 components with a cupro–nickel alloy Cu–30Ni, by DMD process. Cupro–nickel alloys containing 10–30% nickel with some minor alloying additions produced by conventional manufacturing process and some rapid solidification processes have been well researched for their microstructural and mechanical and corrosion property evaluation. However, information on the microstructure and, mechanical and corrosion property of Cu–30Ni alloy deposited by DMD process is not available in open literature. In this investigation, microstructure evolution of Cu–30Ni alloy sample during DMD process and its mechanical and corrosion property evaluation has been reported.

2. Experimental

2.1. Materials

Gas atomized prealloyed Cu–30Ni powder (−100/+325 mesh) (*Michigan Metals & Manufacturing Inc.*) was used for preparing the test specimens Table 1 shows the chemical composition of the as-received powder. Fig. 1(a) shows as-received powder particles morphology and Fig. 1(b) shows particle microstructure. The powder particles were mostly spherical with an average particle size of 75 μm and 85% of the particles within the 60–120 μm range. Approximately 100 particles per micrograph were selected for measurements and always the largest diameter and the diameter in the direction perpendicular to the long axis were measured. The average powder particle porosity was found to be approximately 2%.

2.2. Specimen preparation

Fig. 2 shows the schematic of DMD process. DMD system consists of the laser generation system, the powder delivery system, feedback control system, and CNC motion stage [10]. The DMD process could be performed either in air or under controlled atmosphere. DMD samples for this investigation were prepared at POM using POM DMD 505 machine (developed by POM Group in collaboration with Trumpf Inc.) with a 5 kW CO_2 laser system. A combination of DMD processing parameters: laser power (W), processing speed (mm/min), and, powder feed rates (g/min) and 50% overlap between two adjoining passes, were used to prepare the test specimens. An inert gas mixture of helium and argon provided a protective environment to prevent

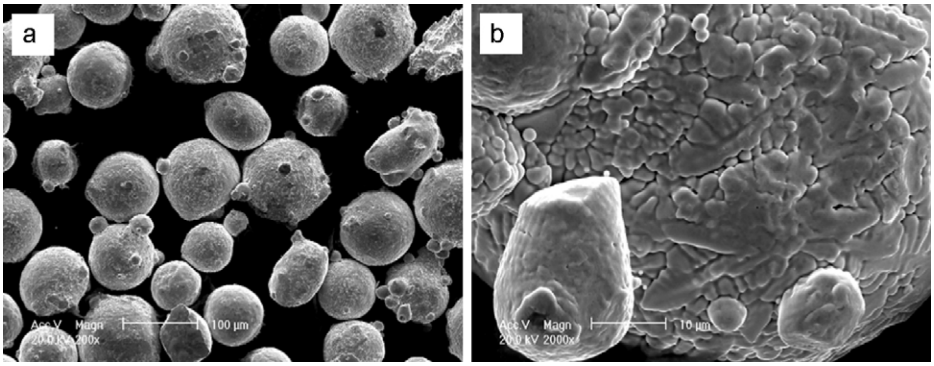

Fig. 1. SEM micrograph of Cu–30Ni alloy powder showing (a) particle morphology (b) particle microstructure.

Table 2
DOE matrix for process parameter optimization of DMD Cu–30Ni alloy.

Run order	Power (W)	Scanning speed (mm min^{-1})	Powder feed rate (g min^{-1})	Layer thickness (mm)	Deposition rate (in.^{3} h^{-1})	Average porosity (%)
1	2500	700	16	0.79	2.02	0.59
2	2000	700	12	0.50	1.28	0.45
3	2500	500	12	0.88	1.61	1.33
4	2000	700	12	0.50	1.28	0.13
5	1500	700	8	0.25	0.64	1.47
6	2500	900	12	0.41	1.35	0.56
7	2000	500	16	0.87	1.59	0.07
8	1500	500	12	0.75	1.37	0.26
9	1500	900	12	0.31	1.02	0.20
10	2000	900	8	0.20	0.66	0.09
11	2000	900	16	0.55	1.81	0.26
12	2000	500	8	0.47	0.86	0.24
13	1500	700	16	0.39	0.99	0.94
14	2500	700	8	0.43	1.09	0.91
15	2000	700	12	0.38	0.96	0.13

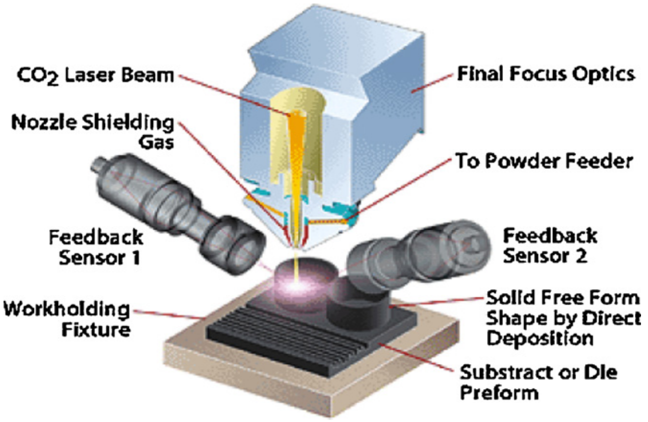

Fig. 2. Schematic diagram showing the DMD process.

Table 3
Optimal parameter combination for depositing DMD Cu–30Ni test specimens.

Sample	Power (W)	Laser spot diameter (mm)	Scanning speed (mm min^{-1})	Powder feed rate (g min^{-1})
Cu–30Ni	2000	2	700	12

oxidation. A 2 mm diameter laser beam with a doughnut-shape power distribution (TEM_{01} mode) was used for all depositions.

Statistical design of experiments (DOE) based on a Surface Response Design Method [23] were performed to optimize the processing parameters for depositing test specimen with minimum porosity and maximum deposition rate. Table 2 shows the DOE matrix for optimizing processing parameters. Table 3 shows the optimal parameter for depositing the test specimen used for microstructural characterization. Rolled C71500 plates were used as the substrates. Test specimen had 16 layers, alloy (or dilution) layer plus 15 layers on top of it. The layers were deposited in a cross hatched pattern, i.e. deposition direction for every layer was perpendicular to the previous layer. Fig. 3 shows the schematic of the clad and the cross hatched pattern deposition scheme. The *Z* increment between layers was approximately 0.5 mm.

2.3. Microstructure characterization and mechanical behavior measurements

Specimens for optical microscopy (OM), and scanning electron microscopy (SEM) observations and microhardness (MH) measurements were obtained from different cross-sections of the experimental specimen. The specimens for OM and SEM were etched with 6 g $FeCl_3$ + 2 g $Fe(NO_3)$ in 200 ml H_2O solution to reveal the microstructure. The microstructure along the longitudinal (*x–z*), transverse (*y–z*) cross-sectional views, and horizontal (*x–y*) (or from top) of the as-deposited test specimens were examined using Nikon^{TM} eclipse ME 600 optical microscope, and a Philips^{TM}, XL30 FEG scanning electron microscope. The crystal structure and the lattice parameter determination was performed by X-ray diffraction (XRD) with a Rigaku rotating anode X-ray diffractometer, and transmission electron microscopy (TEM) with a JEOL 3011 high resolution transmission electron microscope (HRTEM))

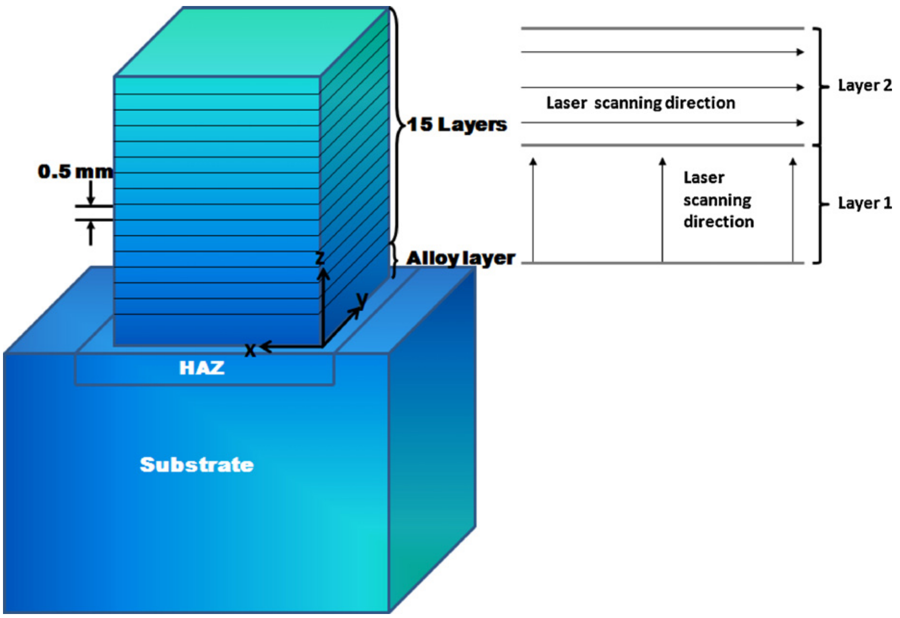

Fig. 3. Schematic showing the deposited layers in DMD specimen and the laser scanning direction in consecutive layers.

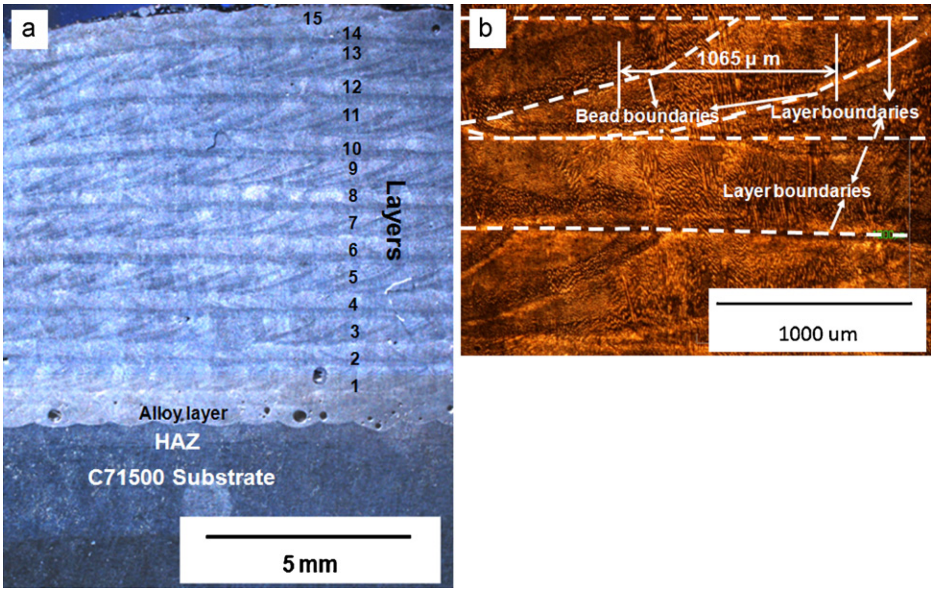

Fig. 4. Optical (a) macrograph showing the deposited layers and the substrate and (b) micrograph showing the layer microstructure of longitudinal cross-section of the DMD Cu–30Ni sample.

operating at 300 kV. Specimen for XRD was obtained from the clad after removing the substrate. XRD was performed with Cu K_α radiation operated at 40 kV and 100 mA, and scanned in the standard θ–2θ range of 35–100° with sampling interval of 0.01°. TEM specimens were prepared from thin slices (300–400 μm thick) taken out of the bulk sample (clad). 3 mm diameter discs were punched out of these slices and these discs were further ground to approximately 30 μm thickness. Thin discs were further thinned or dimpled in the middle by using a dimple grinder (Gatan^{TM} Model 623 Disc Grinder) followed by ion milling (Gatan^{TM} Model 691 Precision Ion Polishing System (PIPS^{TM})) to make them electron transparent.

MH measurements were performed on the polished specimen with a Vickers microhardness tester (Clark, CM-400AT) using 100 g load and dwell time of 15 s. The final hardness across the layers was calculated as the average of three data values.

Mechanical behavior of the clad and the substrate was also compared by tensile testing. Specimens for tensile tests were drawn from C71500 substrate, DMD Cu–30Ni clad and DMD Cu–30Ni/C71500 substrate deposits and prepared following ASTM E8 standard. Five specimens per sample with average gauge length 33 mm, thickness 1.5 mm and reduced cross-section width 6 mm were prepared. Specimens were tested on an Instron® 5982 Universal Testing Instrument with a load cell of 10 kN and loading speed of 3 mm min^{-1}. Fracture surface of tensile specimens were analyzed using SEM.

2.4. Corrosion behavior measurements

Relative corrosion behavior of the substrate and the deposited material was compared by the weight loss measurement during 30 day immersion test, conducted according to ASTM G 31 standard. Test specimens were drawn from C71500 substrate, Cu–30Ni clad and DMD Cu–30Ni/C71500 deposits. Two specimens per test condition with dimensions 50 × 25 × 3 mm (2 × 1 × 1/8 in.) and a hole approximately 8 mm (5/16 in.) diameter for mounting were prepared. The specimens were immersed in synthetic sea water (prepared conforming to ASTM D1141 standard) for 30 days. They were weighed before and after the tests to determine the weight loss. All the immersion tests were conducted at ambient temperatures.

3. Results

3.1. Optical microscopy

Fig. 4(a) shows the optical macrograph of the longitudinal (x–z) cross-section of an as-deposited specimen and Fig. 4(b) shows the optical micrograph of the deposited layers. Thicknesses of alternate layer vary approximately between 475 μm and 620 μm. The Z increment for each layer during deposition was kept at approximately 0.5 mm (500 μm). The laser band width measured from optical micrograph in Fig. 4(b) was found to be approximately 1065 μm. Since the laser beam used for the deposition was 2 mm (or 2000 μm) in diameter it shows that there is approximately 50% overlap between two laser passes. It is to be noted that no feedback control was used during these experiments. The specific energy (or fluence) applied during the deposition and calculated from processing parameters was found to be approximately 86 J/mm^2. In Fig. 5 optical macrographs of (a) longitudinal (x–z) and (b) transverse (y–z) cross-section showing the orientation of laser tracks in each layer with respect to the substrate is presented.

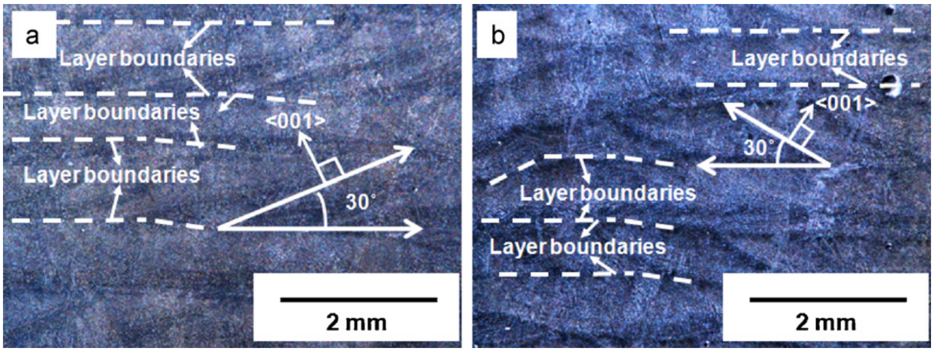

Fig. 5. Optical macrographs of (a) longitudinal (x–z) and (b) transverse (y–z) cross-section of DMD Cu–30Ni clad showing primary dendrite growth direction.

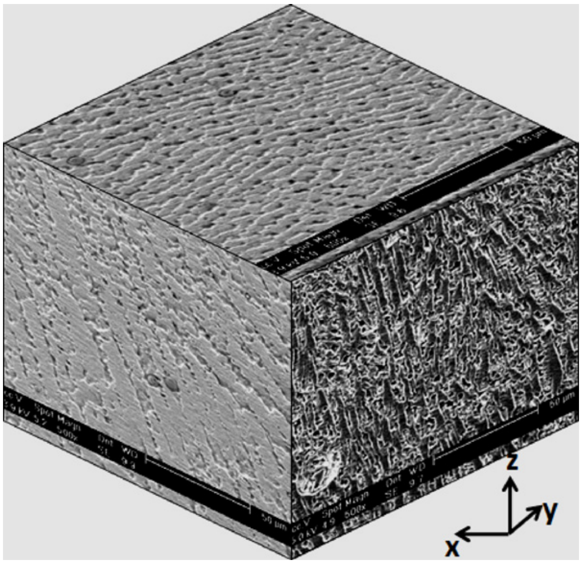

Fig. 6. 3D representation of as-deposited DMD Cu–30Ni sample clad microstructure. The representation was constructed by combining microstructures of the longitudinal and transverse cross-section and plan views.

3.2. Scanning electron microscopy

Fig. 6 shows three-dimensional representation of the microstructure along longitudinal (or x–z) and transverse (or y–z) cross-section views, and plan (or x–y) view of the clad. Fig. 7 shows the orientation directions of dendrites (a) along interface (b) along layer boundaries, and (c) and (d) along bead boundaries. Fig. 8 shows (a) the dendrite growth direction inside a layer and (b) dendrite morphology in the topmost (15th) layer. Fig. 9 shows the microstructure of an individual dendrite with secondary arms and schematic explaining different parts of a dendrite.

Table 4
Average compositions (wt %) obtained from EDAX®.

Scan area	Cu	Ni
Substrate	67.14 ± 0.6	32.86 ± 0.6
Clad	66.33 ± 0.5.	33.67 ± 0.5
Dendrite	63.03 ± 1.0	36.97 ± 1.0
Interdendritic regions	69.49 ± 9.0	30.51 ± 9.0

Table 4 gives the chemical composition obtained from EDAX® analysis of the substrate, clad layers, within individual dendrites and in the interdendritic regions. EDAX® analysis shows that relatively dendrites are richer in nickel than the interdendritic regions.

3.3. X-ray diffraction analysis

Fig. 10 shows the XRD plot of the DMD Cu–30Ni clad. The XRD peaks correspond to a $Cu_{0.5}Ni_{0.5}$ phase with a face centered cubic (FCC) crystal structure. The lattice parameter a calculated from the XRD pattern was 3.5703 Å and that of the phase identified from the powder diffraction file (PDF# 04-004-6750) was 3.5615 Å.

3.4. Transmission electron microscopy

Fig. 11(a) shows the bright field (BF) image of clad with area marked for obtaining selected area diffraction (SAD) and Fig. 11(b) shows the corresponding indexed SAD pattern. SAD pattern confirms that the identified microstructural phase has a FCC crystal structure with a [0 1 1] zone axis (ZA). The lattice parameter a calculated from the SAD pattern was found to be 3.5700 Å. This value is approximately 2.4% longer than the reported lattice parameter (3.5615 Å) of the identified phase (PDF# 04-004-6750) matching the XRD pattern. It was however very close, (0.0084% shorter) to the lattice parameter value calculated from the XRD pattern. It is to be noted that the lattice parameter values obtained from powder diffraction files (PDF) of phases matching the XRD patterns are obtained from equilibrium microstructures.

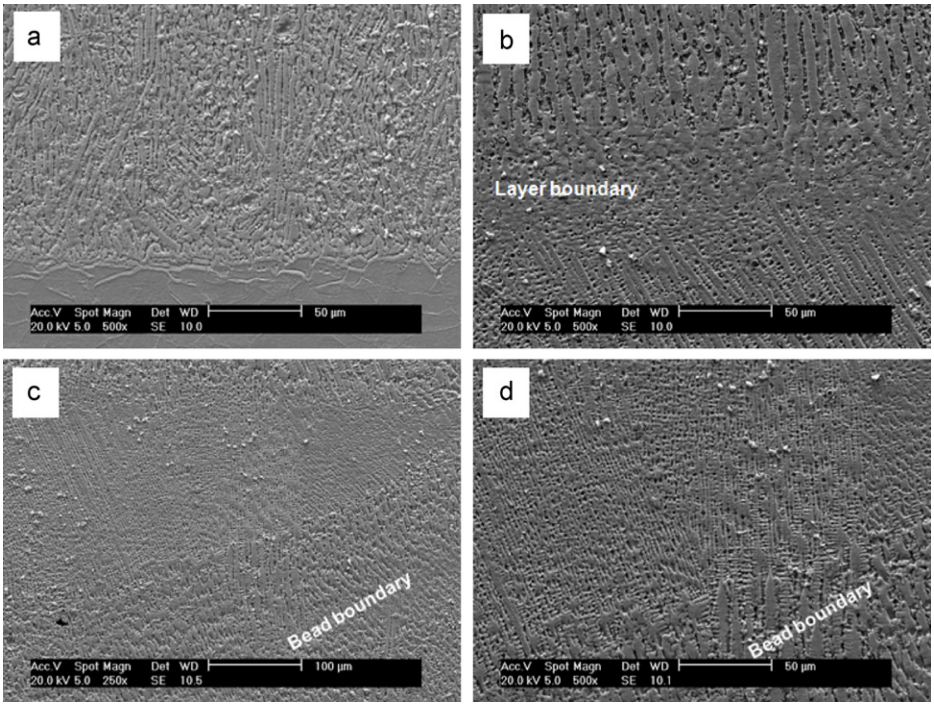

Fig. 7. SEM micrographs of longitudinal cross-section of DMD Cu–30Ni sample showing growth direction of dendrites (a) from interface, (b) from layer boundaries, and (c) and (d) from bead boundaries.

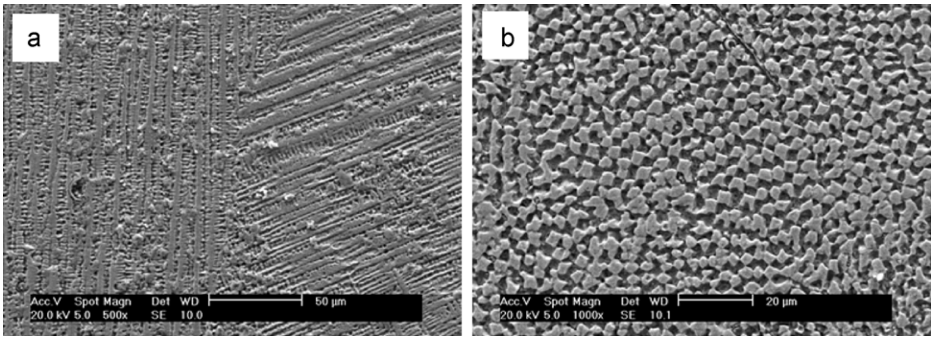

Fig. 8. SEM micrographs of longitudinal cross-section of DMD Cu–30Ni sample showing (a) dendrite growth direction inside a layer and (b) dendrite morphology in the top (15th layer).

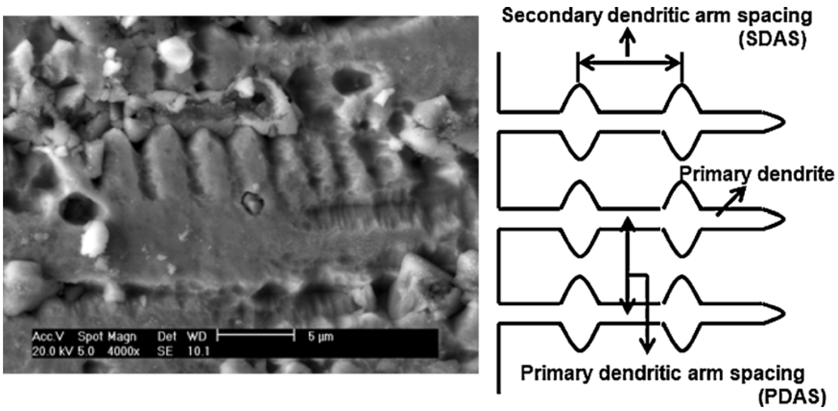

Fig. 9. SEM micrograph showing an individual dendrite and a schematic showing different sections of dendrites with secondary arms.

3.5. Microhardness measurement

MH measurements were taken across the specimen, from substrate to the top clad layer (layer 15). Fig. 12 shows the microhardness plotted against distance from the interface. Microhardness values were found to decrease from substrate to the clad. However, clad microhardness was found to be very consistent and vary between 115 and 130 HVN.

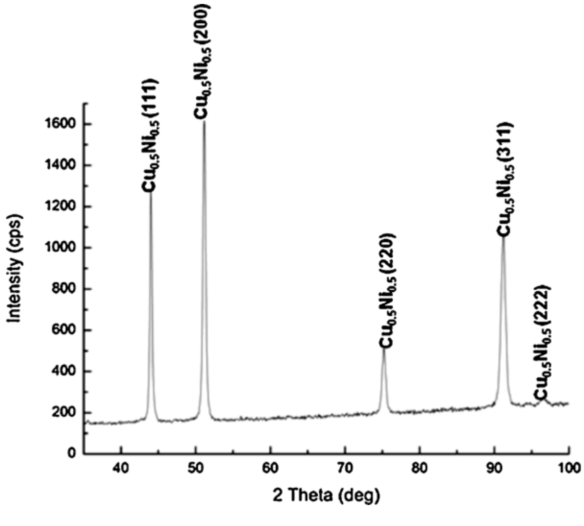

Fig. 10. XRD scan of DMD Cu–30Ni sample.

3.6. Tensile properties measurements

Table 5 shows the tensile properties of the DMD Cu–30Ni clad, C71500 substrate and DMD Cu–30Ni clad/C71500 substrate specimens. It was observed that the DMD Cu–30Ni clad specimens had higher ultimate tensile strength (UTS) but lower yield strength (YS) and percentage (%) elongation as compared to the C71500 substrate specimens. However, tensile properties of DMD Cu–30Ni clad/C71500 substrate specimens were lower than both clad and substrate.

3.7. Fracture surface micrographs

Fig. 13 shows the fractographs of the tensile specimen showing (a) overall fracture cross-section, (b) magnified view of the clad fracture cross-section, and (c) and (d) magnified view of the substrate fracture cross-section. Both equiaxed and elongated dimple like depressions were observed in all the tensile specimen fractographs. Fig. 13(d) also shows some smooth rippled surfaces in the substrate fractographs. Porosities were also observed in the clad and substrate fractographs.

Table 5
Room temperature tensile properties of Cu–30Ni clad, C71500 substrate and DMD Cu–30Ni/C71500 substrate specimens.

Specimen	UTS (MPa)	YS (MPa)	% Elongation
DMD Cu–30Ni clad	240.49	317.16	13.9
C71500 substrate	233.39	374.90	31.5
DMD Cu–30Ni clad/C71500 substrate	258.72	229.08	3.37

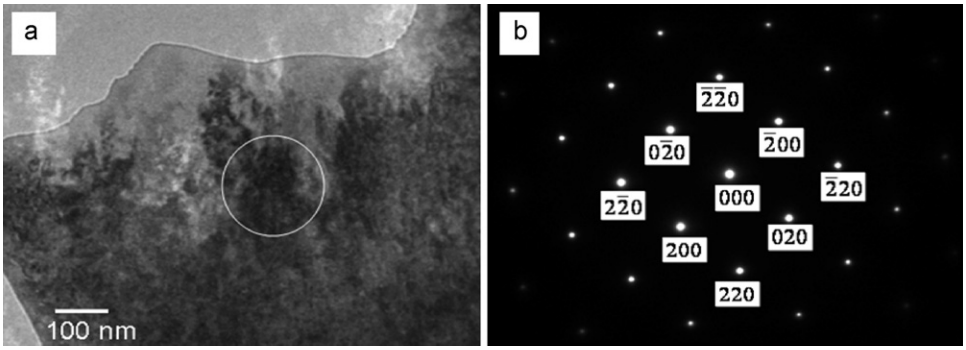

Fig. 11. (a) Bright field image showing the area marked for SAD pattern and (b) corresponding indexed SAD pattern.

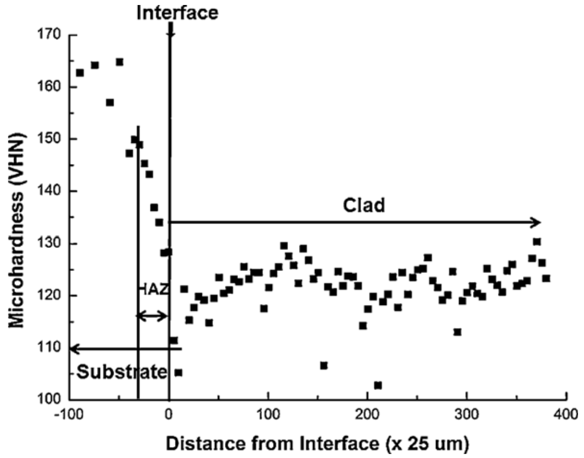

Fig. 12. Plot showing variation of microhardness with distance from interface.

3.8. Corrosion behavior measurements

Table 6 shows the results from 30 day immersion test. Corrosion rate of the specimens was found to decrease in the order: DMD Cu–30Ni clad, DMD Cu–30Ni clad/C71500 substrate, C71500 substrate. General corrosion was observed in all samples but no corrosion pits were detected.

4. Discussion

4.1. Deposition quality evaluation

Fig. 4(a) shows the optical macrograph of the longitudinal (*x*–*y*) cross-section of the clad. The deposition quality was found to be sound with no cracks or non-bonding at the interfaces and less than 2% clad porosity, which could be safely attributed to powder particle porosity. This shows that Cu–30Ni alloy is a suitable material for DMD.

4.2. Solidification mechanism

Fig. 14 [24] shows the copper–nickel binary alloy phase diagram and the approximate alloy composition is indicated by an arrow. It is known that copper–nickel alloys form series of substitutional solid solutions over the entire composition range. This is possible since both copper and nickel have face-centered cubic crystal structure and their atomic volume differ by only 2.5% [25].

Table 6
Corrosion rate from 30 day immersion test.

Specimen	Corrosion rate (mpy)
Cu–30Ni clad	0.36
DMD Cu–30Ni/C71500	0.2
C71500 substrate	0.08

During solidification in alloys, both thermal and compositional gradients and considerable undercooling below the melting temperature exists across the solidification front. It is known that constitutional undercooling is created by the thermal gradients and it destabilizes the solid/liquid (S/L) interface and creates interface morphologies. For a given alloy composition, solidification morphology depends on parameters such as, thermal gradient, G (in the liquid at the S/L interface) and solidification velocity (V). The ratio G/V influences the S/L interface instability and eventually microstructure morphologies. The ratio G/V and constitutional undercooling ΔT are related by the equation $G/V < \Delta T/D$, where D is the liquid diffusivity. As the ratio decreases, S/L instability increases resulting in the formation of planar to cellular to dendrite to equiaxed dendrite structures [26].

In DMD at the substrate solidification starts at the bottom of the melt pool, where V is zero and G has the highest value, so the G/V ratio is infinite. It has been reported that V increases and G decreases rapidly with height and hence the ratio decreases from the bottom to the top of the melt pool finally stabilizing at the surface. Hence the bottom of the melt pool has a planar structure, gradually developing into cellular to dendritic structure, which gets finer finally transforming into equiaxed dendrites on moving away from the bottom [27,28]. Due to rapid solidification, planar and cellular structures exist over a very narrow zone and final structure is mostly dendritic with the growth direction away from the substrate as seen from Fig. 7(a).

4.3. Dendrite growth, morphology and composition evaluation

Fig. 6 shows an overall morphology of deposited layers. The representation was constructed by combining microstructures of the longitudinal and transverse cross-sectional and planar views. As seen from this isometric or 3D view, clad microstructure primarily consists of columnar dendrites which were formed by the epitaxial growth of primary dendrites at the substrate and partially remelted previously deposited layer and bead boundaries. During DMD, substrate and deposited layers act as the heat sink and as mentioned earlier solidification initiates by epitaxial growth from the substrate and boundaries. This causes directional solidification and subsequent growth of columnar structure occur counter to the heat flux direction [4,29]. It has been reported [29,30] and was also found in this investigation (Fig. 7(a)) that the columnar grain growth direction is mostly normal to the substrate. However in each layer, growth direction of primary dendrites from layer boundaries depends on the laser scanning direction and in the current investigation it was found that primary dendrites were

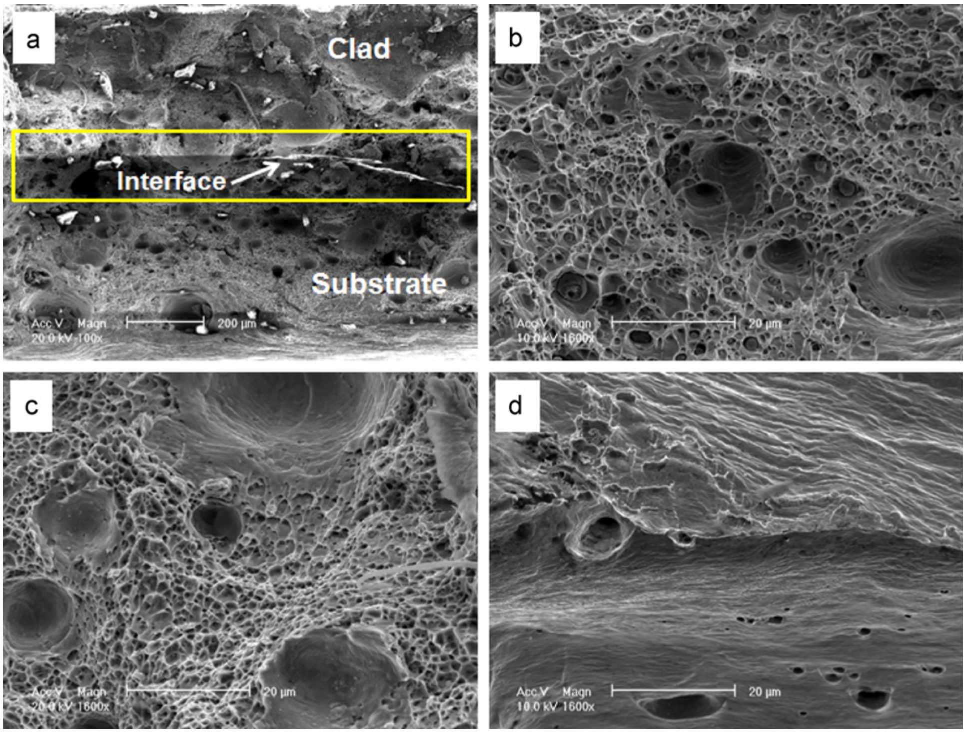

Fig. 13. Fractographs of the tensile specimen showing (a) the overall surface, (b) magnified view of the clad, and (c) and (d) magnified view of the substrate.

at approximately 60° with the substrate and when the laser scan direction changed this angle was maintained (Fig. 5). In general it was observed that layer and bead boundaries consisted of columnar dendrites with often no secondary dendritic arms. Very large value of G/V at the bottom of the melt pool did not allow the growth of secondary dendrites. As the ratio decreases from the bottom to the top of the melt pool, the microstructure transformed from fully columnar at the layer boundaries to dendrites with secondary arms which became finer as they moved away from the boundaries (Fig. 7). Fig. 7(b) shows the remelted layer boundary and the dendrites growing away from the boundary. The remelting of layer boundaries was caused by the overlap of layers during deposition.

It is well known that in cubic crystals primary dendrites grow along the preferred crystallographic orientation i.e. ⟨001⟩ direction closest to the heat flux direction [29], as seen in Fig. 5. Dendrite growth directions inside a layer also depends on localized heat conduction and are not always absolutely parallel to each other as was observed in Figs. 7(d) and 8(a). In Fig. 8(a) it is observed that dendrites changed their orientation and are at certain angle with each other. This transition can be attributed to localized heat flux direction and also layer overlap. Fig. 8(b) shows the microstructure of the topmost (15th) layer which consisted of equiaxed dendrites. This could be explained based on solidification velocity and constitutional undercooling at the top of the melt pool. As at the G/V ratio is very small at the top of the melt pool and also there is greater constitutional undercooling compared to the bottom which results in columnar to equiaxed dendrite microstructure transformation. The uppermost part of every layer is expected to have this structure, but was only observed in the topmost layer since there was considerable amount of overlap in the deposited bottom layers. Fig. 9 shows the micrograph of a single dendrite and a schematic explaining the dendritic morphology. Dinda et al. [4] stated that the secondary dendrites are nearly perpendicular to the primary dendrites and served as the growth sites for the primary dendrites of the next layer as they follow the heat flux direction. This probably helped to maintain the growth direction of primary dendrites in subsequent layers. The average primary dendritic arm spacing (PDAS) at the bottom part of the layers was about 7.5 µm and average secondary dendritic arm spacing (SDAS) in the upper part of the layer varied between 2 µm and 4.5 µm.

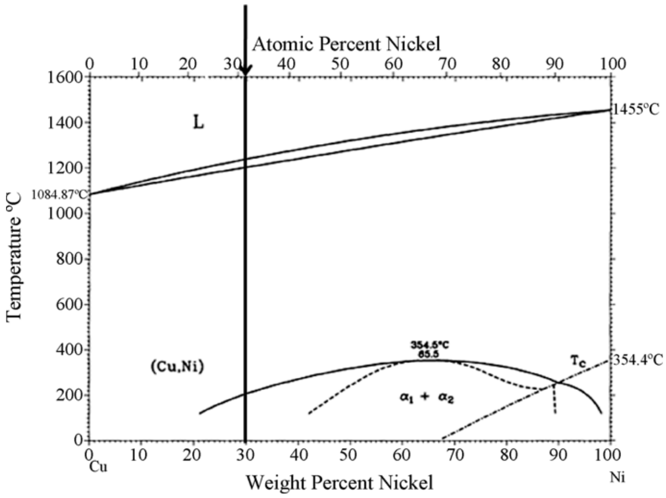

Fig. 14. Binary alloy phase diagram of copper and nickel [24].

During solidification rejection of solute from the solid into the solidifying liquid produces compositional inhomogeneity across the dendrite and causes micro-segregation. However, during rapid solidification processes such as DMD large undercooling results in solidification velocity to exceed the diffusive speeds of solute atoms. As a result, these solute atoms get trapped in the solid beyond their equilibrium solubility [5] and sometimes produce micro-segregation free structures. EDAX® compositional analysis of the dendrites and interdendritic regions in Table 3 shows similar results. The dendrites are relatively richer in solute nickel compared to the interdendritic regions. It should be noted that the compositions given are average values of measurements taken over several areas, since the interaction volume of electron beam used during EDAX® analysis could be larger than the actual area being scanned.

4.4. Crystal structure evaluation

The lattice parameter calculated from the XRD pattern (Fig. 10) was found to be 3.5703 Å and the lattice parameter of the identified $Cu_{0.5}Ni_{0.5}$ solid solution phase matching the XRD pattern (PDF# 04-004-6750) was found to be 3.5615 Å. The lattice parameter of the FCC phase calculated from the SAD pattern was found to be 3.570 Å. This value is approximately 0.008% shorter than the lattice parameter value obtained from the XRD pattern and 2.4% longer than the lattice parameter value obtained from the PDF file of the identified phase. The lattice parameter calculated from SAD pattern also agrees closely with the lattice parameter calculation from the powder composition following Vegard's law. Vegard's law states that the effective lattice parameter of a binary solid solution can be expected as the linear sum of the weighted means of the lattice parameters of the solute and the solvent [31]. The lattice parameters of pure copper and pure nickel obtained from literature are 3.610 Å and 3.540 Å respectively. In the current investigation lattice parameter calculated from the powder composition, considering only the weight percentages of copper and nickel, 70 and 30 respectively was 3.590 Å. As mentioned earlier, rapid solidification during DMD results in residual stress development in clads. The residual stresses in DMD materials are primarily developed due to plastic deformation occurring during thermal expansion and/or and volumetric changes during phase transformations [11]. These residual stresses, are tensile in nature except for the austenite to martensite transformation in certain steels where compressive stresses are developed [32,33] and affect the crystal structure of microstructural phases [34]. Increase in lattice parameter of the solid solution phase could be safely attributed to the residual stress developed in the clad. It should be noted that the PDF files are obtained from materials processed under equilibrium conditions.

4.5. Mechanical property evaluation

Microhardness of the clad was found to be lower than the substrate. The substrate used is a rolled sheet which was work hardened by cold rolling and hence has a higher hardness compared to the clad. However, the closely consistent microhardness of the clad proves the homogeneity of the microstructure. In general, microhardness and tensile properties of rapidly solidified cupro–nickel alloys have been reported to be higher than the sand cast alloys [19,20].

Tensile test results showed that the DMD Cu–30Ni clad specimen had higher UTS but lower YS and % elongation compared to the C71500 substrate specimen. DMD Cu–30Ni clad/C71500 substrate specimen had the lowest tensile properties among all the specimens. Lower tensile properties of DMD Cu–30Ni clad/C71500 substrate specimen could be attributed to the porosity observed in the alloy layer.

4.6. Fractography and failure mode analysis

Primarily cup like depressions in the fractographs suggest that the failure occurred by dimple fracture and the material exhibits ductility. It is reported that overload is the principal cause of formation of dimple ruptures and failure in most common alloys have occurred by the mechanism known as microvoid coalescence. Microvoids nucleate at sites with localized strain discontinuities and grow and coalesce with the increase in strain eventually leading to the dimple fracture [35]. Fig. 14(b) shows the substrate cross-section fractograph with a type of dimple fracture known as serpentine glide or riples. This type of fracture is observed in metals with high ductility. Slip planes at the surface of large dimples, oriented along to the major stress direction produce deformation tracks on the dimple walls. Continual straining causes displacement of these slips planes. The tracks produced by these displacements initially appear as sharp well defined pattern called serpentine glide, and with further straining evolve into smooth wavy surface called riples [35]. Porosities observed in the clad and substrate fractographs could also act as sites of localized strain discontinuities. Besides porosities mixed dimple fracture modes observed in the DMD Cu–30Ni clad/C71500 substrate specimens correlates to the observed lower tensile properties.

4.7. Corrosion property evaluation

The corrosion resistance of DMD Cu–30Ni clad specimen was found to be lower than the C71500 substrate, but was found to improve in case of DMD Cu–30Ni clad/C71500 substrate specimen. The porosity in the clad is probably the cause for higher corrosion rate. Lower corrosion rate in half and half specimens indicates that the strong interface was very effective in increasing the corrosion resistance of the specimen. Small amount of clad porosity probably increased the corrosion rate of the DMD Cu–30Ni clad specimens. In general, corrosion resistance of cupro–nickel alloys produced by rapid solidification has been reported to be higher than their cast counterparts [20]. Also the corrosion resistance of cupro–nickel alloys produced by conventional methods has also shown to have improved with heat treatment [12,13].

5. Conclusion

Cu–30Ni alloy was successfully deposited on a C71500 substrate using a DMD system with CO_2 laser. The specimen consisted of an alloy layer and 15 layers on top of the alloy layer. The microstructure consists of a single solid solution phase. The layer microstructure primarily consists of columnar dendrites in the bottom growing into equiaxed dendrites at the top. Dendrites grew epitaxially from substrate, and layer and bead boundaries. Dendrite growth direction ($\langle 0\,0\,1\rangle$) and growth angle (60°) with respect to the substrate was maintained in each layer. The average primary dendritic arm spacing at the bottom part of the layers was about 7.5 μm and average secondary dendritic arm spacing in the upper part of the layer varied between 2 μm and 4.5 μm. The identified solid solution phase from TEM SAD pattern had a FCC crystal structure with a lattice parameter of 3.570 Å which is approximately 2.4% longer than the lattice parameter value 3.5615 Å obtained from the PDF file matching the XRD pattern. However, it was found to be very close to the lattice parameter value obtained from the XRD pattern itself. The microhardness of the clad was found to be less than the substrate but was very consistent along the clad. Cu–30Ni clad specimen showed higher ultimate tensile strength but lower yield strength and % elongation as compared to the C71500 substrate. The corrosion resistance of DMD Cu–30Ni clad specimen was found to be lower than the C71500 substrate, but was found to improve in case of DMD Cu–30Ni clad/C71500 substrate specimen. Clad porosity could be the reason for higher corrosion rate of the DMD Cu–30Ni clad specimens.

Acknowledgements

The current investigation was financially supported by the Office of Naval Research. Authors would like to thank Dr. Kai Sun from the Electron Microscope Analysis Laboratory (EMAL) at University of Michigan and the colleagues from Focus: HOPE for their help in this work.

References

[1] J. Mazumder, J. Choi, K. Nagarathnam, J. Koch, D. Hetzner, JOM 49 (1997) 55–60.
[2] J. Mazumder, A. Schifferer, J. Choi, Mater. Res. Innovations 3 (1999) 118–131.
[3] J. Mazumder, D. Dutta, N. Kikuchi, A. Ghosh, Opt. Lasers Eng. 34 (2000) 397–414.
[4] G.P. Dinda, A.K. Dasgupta, J. Mazumder, Mater. Sci. Eng. A 509 (2009) 98–104.
[5] J. Singh, J. Mazumder, Acta Metall. 35 (1987) 1995–2003.
[6] J.O. Milewski, G.K. Lewis, D.J. Thoma, G.I. Keel, R.B. Nemec, R.A. Reinert, J. Mater. Process. Technol. 75 (1998) 165–172.
[7] http://www.sandia.gov/mst/pdf/LENS.pdf.
[8] D.E. Bunnell, D.L. Bourell, H.L. Marcus, Proceedings of the 1996 International Conference on Powder Metallurgy and Particulate Materials, Metal Powders Industries Federation, Princeton, NJ, Section 15, 1996, pp. 93–106.
[9] L. Costa, R. Vilar, Rapid Prototyping J. 15 (2009) 264–279.
[10] J.L. Koch, J. Mazumder: U.S. Patent Number 6,122,564, September 19, 2000.
[11] P.B. Kadolkar, T.R. Watkins, J.Th.M. De Hosson, B.J. Kooi, N.B. Dahotre, Acta Mater. 55 (2007) 1203–1214.
[12] X. Mao, F. Fang, F. Yang, J. Jiang, R. Tan, J. Mater. Process. Technol. 209 (2009) 2145–2151.
[13] Z. Jie, W. Qing, W. Yingmin, W. Lishi, D. Chuang, J. Alloys Compd. 505 (2010) 505–509.
[14] L.J.P. Drolenga, F.P. Ijsseling, B.H. Kolster, Mater. Corros. 34 (1983) 167–178.
[15] S. Kang, P.K. Domalavage, N.J. Grant, Mater. Sci. Eng. 78 (1986) 33–44.
[16] L.J. Swartzendruber, L.H. Bennett, Scripta Metall. Mater. 2 (1968) 93–98.
[17] J.M. Popplewell, R.J. Hart, J.A. Ford, Corros. Sci. 13 (1973) 295–309.
[18] J.M. Popplewell, Corros. Sci. 13 (1973) 593–603.
[19] S.H. Lo, W.M. Gibbon, R.S. Holliongshead, J. Mater. Sci. 22 (1987) 3293–3296.
[20] D. Baril, R. Angers, J. Baril, Mater. Sci. Eng. 158 (1992) 7–10.
[21] N.W. Polan, M.A. Heine, J.M. Popplewell, C.J. Gaffoglio, Desalination 38 (1981) 223–231.
[22] A.N. Beccaria, G. Poggio, P. Traverso, M. Ghiazza, Corros. Sci. 32 (1991) 1263–1275.
[23] http://www.itl.nist.gov/div898/handbook/pri/section3/pri3363.htm.
[24] ASM Handbook Online, ASM International, 3 (1992).
[25] R.N. Caron, R.G. Barth, D.E. Tyler, ASM Handbook, vol. 9, ASM International, 2004, pp. 775–788.
[26] D.M. Stefanescu, R. Ruxanda, ASM Handbook, vol. 9, ASM International, 2004, pp. 71–92.
[27] W. Kurz, R. Trivedi, Mater. Sci. Eng. A 179–180 (1994) 46–51.
[28] R. Vilar, Int. J. Powder Metall. 37 (2001) 31–48.
[29] M. Gäumann, S. Henry, F. Cléton, J.-D. Wagnière, W. Kurz, Mater. Sci. Eng. A 271 (1999) 232–241.
[30] M. Gäumann, C. Bezençon, P. Canalis, W. Kurz, Acta Mater. 49 (2001) 1051–1062.
[31] V.A. Lubarda, Mech. Mater. 35 (2003) 53–68.
[32] M.R. James, D.S. Gnanamuthu, R.J. Moores, Scripta Metall. Mater. 18 (1984) 357–361.
[33] M. R-Fishman, L.S. Zevin, J. Zahavi, J. Mater. Sci. Lett. 7 (1988) 741–744.
[34] S. Bhattacharya, G.P. Dinda, A.K. Dasgupta, J. Mazumder, Mater. Sci. Eng. A 528 (2011) 2309–2318.
[35] V. Kerlins, ASM Handbook, vol. 12, ASM International, 1987.